Journal of Environmental Chemical Engineering 11 (2023) 110209

Contents lists available at ScienceDirect

Journal of Environmental Chemical Engineering

journal homepage: www.elsevier.com/locate/jece

Photo, thermal and photothermal activity of TiO_2 supported Pt catalysts for plasmon-driven environmental applications

Gregor Žerjav [a,*], Zafer Say [b], Janez Zavašnik [c], Matjaž Finšgar [d], Christoph Langhammer [b], Albin Pintar [a]

[a] Department of Inorganic Chemistry and Technology, National Institute of Chemistry, Hajdrihova 19, SI-1001 Ljubljana, Slovenia
[b] Department of Physics, Chalmers University of Technology, Gothenburg SE-412-96, Sweden
[c] Gaseous Electronics, Jožef Stefan Institute, Jamova cesta 39, SI-1000 Ljubljana, Slovenia
[d] University of Maribor, Faculty of Chemistry and Chemical Engineering, Smetanova ulica 17, SI-2000 Maribor, Slovenia

ARTICLE INFO

Editor: Javier Marugan

Keywords:
Heterogeneous photocatalysis
TiO_2
Plasmonic noble metal
Pt particles
Visible-light illumination
Schottky barrier height
Bisphenol A
Wastewater treatment
NO_x abatement
Air cleaning
Microreactor
Thermal catalysis
Photothermal catalysis
H_2-deNO_x

ABSTRACT

TiO_2+Pt plasmonic solids with 1 wt% Pt and different TiO_2 supports (anatase nanoparticles (TNP), polycrystalline nanorods (a-TNR) and single-crystal anatase nanorods (TNR)) were synthesized using the wet impregnation technique and tested as photo, thermal and photothermal catalysts in gas-solid and gas-liquid-solid reactions. Due to the different charges of the TiO_2 support surfaces, Pt particles with different sizes, crystallinities and degrees of interaction with the TiO_2 supports were formed during the synthesis. The heights of the Schottky barrier (SBH) were 0.38 eV for the a-TNR+Pt, 0.41 eV for the TNP+Pt, and 0.50 eV for the TNR+Pt samples, respectively. The low visible-light-triggered photocatalytic activity of the TNR+Pt catalyst toward the oxidation of water-dissolved bisphenol A (BPA) is attributed to its high SBH and active site deactivation due to the adsorption of BPA and/or BPA oxidation products. The highest photothermal catalytic H_2-assisted NO_2 reduction rate was expressed by the TNR+Pt catalyst. This can be ascribed to the presence of a narrow particle size distribution of small Pt particles, the absence of the Pt catalysed reduction of the TNR support at higher temperatures, and the lower rate of re-injection of "hot electrons" from the TNR support to the Pt particles.

1. Introduction

The socio-economic development in the past decades has increased organic wastewater pollution with a huge impact on human health [1, 2]. Wastewater treatment technologies can be classified into physical (sedimentation, adsorption, membrane separation), biological (activated sludge and biofilm) and chemical treatment methods [3–6]. The advantage of the chemical treatment methods is that they can rapidly oxidize and completely degrade the organic pollutants without producing secondary waste products [7]. Advanced oxidation processes (AOPs), including Fenton oxidation, photocatalytic oxidation, catalytic wet air oxidation (CWAO), etc., especially exhibit high oxidation reaction rates, high mineralization efficiency, and a low level of secondary pollutant production [8–10]. Through the generation of highly active reactive oxygen species (ROS, hydroxyl radicals (•OH), superoxide radicals ($O_2^{\bullet-}$), etc.), the AOPs can fully degrade organic pollutants into CO_2 and H_2O in the final process called mineralization. Among the AOPs, photocatalytic oxidation technology is especially considered an energy-saving green technology to treat organically polluted wastewater as only a photocatalyst and illumination with light are required, with no need for the addition of chemical agents, such as ozone. Photocatalysts, most commonly semiconductors, are used that upon illumination with light, the energy of which is the same or higher than the band gap energy of the catalyst, produce electrons (e^-) and holes (h^+). The generated charge carriers are further used to directly degrade water-dissolved organic pollutants or to produce ROS. The generated charge carriers can also be recombined to produce heat, but then they cannot be used for the degradation of organic pollutants in wastewater.

* Corresponding author.
E-mail address: gregor.zerjav@ki.si (G. Žerjav).

https://doi.org/10.1016/j.jece.2023.110209
Received 18 April 2023; Received in revised form 23 May 2023; Accepted 25 May 2023
Available online 26 May 2023

Two factors determine the quantum efficiency of a photocatalytic material. The first is the electron-hole pair recombination rate and the second is the light utilization efficiency. The quantum efficiency of the most commonly used and investigated photocatalyst in heterogeneous photocatalysis, titanium dioxide (TiO_2), suffers from its two major drawbacks, namely a high electron-hole recombination rate and a high band gap energy (3.0–3.4 eV) [11]. Due to this, only UV-light illumination can be employed to trigger TiO_2 to generate charge carriers, which makes the photocatalytic process cost-ineffective. Different approaches/methods can be used to improve the quantum efficiency, for example, (i) forming a heterojunction with another semiconductor [12–14], (ii) elemental doping [15], (iii) morphology control [16], (iv) the deposition of noble plasmonic metals (PM; Au, Ag, Pd, Pt) [17,18], etc. The deposition of a noble metal onto TiO_2 enables the generation of charge carriers under visible-light illumination due to the localized surface plasmon resonance (LSPR) effect expressed by the PM [19]. Further, an electronic potential barrier, the so-called Schottky barrier (SB), is formed at the noble metal-semiconductor heterojunction, which inhibits the recombination of the visible-light-generated charge carriers and promotes the interfacial charge transfer [20]. Žerjav et al. [18] reported that the selection of the TiO_2 support could significantly influence the properties of the TiO_2 +PM photocatalysts and their photocatalytic activity.

Furthermore, the anthropogenic activities in recent decades have not only influenced the quality of aquatic bodies but also led to high emissions of nitrogen oxides (NO_x) into the atmosphere, which can significantly impact animal and human health and vegetation [21]. Due to the presence of NO_x, especially NO and NO_2, various environmental problems can be created, such as the formation of acid rain, photochemical smog, greenhouse effect etc. NO_x present in the atmosphere can further react with other air pollutants (volatile organic compounds (VOC)) and form products (for example, peroxyacyl nitrate (PANI), nitrous acid, etc.) that are even more harmful to humans than NO_x [22]. The NO_x removal methods can be divided into primary and secondary procedures [23]. The primary NO_x removal methods are carried out inside a combustion zone (for example, a furnace) without the need for another reactor and the NO_x reduction is maintained/directed by the adjustment of the combustion parameters. The most commonly used secondary NO_x removal methods are selective catalytic reduction (SCR) and selective non-catalytic reduction (SNCR) [24,25]. The SCR is realized by introducing different reducing agents (e.g. H_2, CO, NH_3, HC, etc.) and usually occurs on the catalyst surface at between 300 and 400 °C. The disadvantages of using HC and NH_3 in SCR are poor low-temperature activity and the deterioration of the catalysts [26–28]. The advantage of using H_2 as a reducing agent is that it can reduce NO_x at relatively low temperatures and produces low emissions of greenhouse gasses [29,30]. In the past, researchers demonstrated [31,32] that supported Pt catalysts exhibited activity toward the H_2-assisted NO_x-SCR, although the deNO_x activity at low temperatures (<200 °C) should be improved [33]. The improvement of the low-temperature deNO_x activity of catalysts can be, for instance, achieved by the use of a photothermal catalytic process, which is a hybrid technology where the advantages of thermal and photo-based catalytic approaches are synergistically combined [34–36]. The materials used as a catalyst in photothermal catalysis should function as a photo and as a thermal catalyst. It was reported that TiO_2 +Pt-based materials displayed activity under hybrid photothermal conditions as both photo and thermal catalysts [37].

The aim of the present study was to investigate in detail how the optical, electronic and catalytic properties of TiO_2 +Pt catalysts with 1 wt% Pt loading depend on the textural and morphological properties of the TiO_2 support. For this purpose, we used three different TiO_2 supports, i.e. anatase nanoparticles (TNP), polycrystalline nanorods (a-TNR) and single-crystal anatase nanorods (TNR). Special attention in this work was given to the use of the X-ray photoelectron spectroscopy (XPS) technique to determine the height of SB (SBH) in the investigated materials and to correlate it with the photocatalytic activity of TiO_2 +Pt catalysts. Furthermore, the aim was also to investigate the multifunctional use of the prepared catalysts by using the same material as a photo, thermal and photothermal catalyst in various environmental cleaning applications. The ability of the synthesized TiO_2 +Pt materials to be used as a photocatalyst for the wastewater treatment was tested in a batch slurry reactor under visible-light illumination using water-dissolved bisphenol A (BPA) as a model organic pollutant. In addition, the prepared solids were examined in a catalytic model reaction to evaluate the activity during NO_x reduction in the presence of H_2 as a reducing agent, conceptually demonstrating an alternative approach for low-temperature NO_x abatement that was further enhanced/upgraded by photocatalysis where visible-light illumination was employed.

2. Experimental

2.1. Catalyst synthesis

Three different TiO_2 supports were used in a wet-impregnation synthesis procedure to prepare TiO_2 +Pt catalysts. At first, we used the commercially available TiO_2 support DT-51 (donated by CristalACTRiV™, France), which is denoted as TNP (TiO_2 nanoparticles). TNP was also used in a hydrothermal procedure [14] to prepare the second TiO_2 support, polycrystalline TiO_2 nanorods (denoted as a-TNR). The third TiO_2 support prepared in this study was a-TNR calcined at 500 °C for 2 h so that the polycrystalline TiO_2 nanorods transformed into single-crystal anatase TiO_2 nanorods (denoted as TNR). To obtain TiO_2 +Pt catalysts with 1 wt% of Pt loading, 1 g of TiO_2 support was added to a diamminedinitritoplatinum(II) ($Pt(NH_3)_2(NO_2)_2$) aqueous solution (50 ml) and stirred for 20 h. After drying overnight at 60 °C, the samples were calcined at 450 °C for 3 h (heat ramp 10 °C/min). The prepared TiO_2 +Pt catalysts were denoted as TNP+Pt, a-TNR+Pt and TNR+Pt.

2.2. SEM, N_2 physisorption, XRD, zeta potential, H_2-TPD and Pt dispersion analyses

The morphology and chemical composition of the synthesised TiO_2 +Pt catalysts were analysed using a field-emission scanning electron microscope (FE-SEM, SUPRA 35 VP, Carl Zeiss) equipped with an energy-dispersive X-ray spectrometer (EDS, model Inca 400, Oxford Instruments). Further, the crystal structure and phase composition were assessed using a transmission electron microscope (TEM, JEM-2100, JEOL) operating at 200 keV. The micrographs were recorded by a high-resolution slow-scan CCD camera (Orius SC1000, Gatan Inc.).

The N_2 adsorption/desorption isotherms of the materials were obtained at − 196°C with the use of Micromeritics' TriStar II 3020 analyser. Prior to the measurements, the samples were pre-treated in Micromeritics' SmartPrep degasser in a stream of N_2 (Linde, purity 6.0) for 60 min at 90 °C and further for 240 min at 180 °C.

The phase composition of the prepared catalysts was measured using an X-ray powder diffraction diffractometer (XRD, X'pert PRO MPD, PANalytical) utilising Cu $K\alpha_1$ radiation (λ = 1.54056 Å) in reflection geometry between 10 and 90° and steps of 0.0341°. The results were interpreted using a PDF database from the International Centre for Diffraction Data (ICDD).

A Malvern Panalytical Ultra Red zetasizer equipped with an automatic titration device was used to determine the zeta potential of the investigated bare TiO_2 supports in the pH range from 2 to 9 using HCl and NaOH solutions to control the pH value. Before the measurements, 25 mg of the investigated TiO_2 supports were dispersed for 30 min in 100 ml of distilled water using an IKA Lab Disc ultra-flat stirrer.

An AutoChem II 2920 apparatus from Micromeritics, fitted with a Thermal Conductivity Detector (TCD), was employed to perform temperature-programmed reduction analysis (H_2-TPR) of the prepared catalysts. During the measurement, 100 mg of the sample was positioned on a quartz wool flock inside a U-shaped quartz tube and pre-treated in 5% O_2/He at 350 °C for 10 min, followed by cooling to − 50 °C. After 5

min, the flow was changed to 5% H_2/Ar and a linear temperature ramp of 10 °C/min was employed until the final temperature of 550 °C was reached.

CO chemisorption analysis was performed using a Micromeritics AutoChem II 2920 instrument. The catalyst samples were weighed (150 mg each) and placed on a quartz wool flock plugged in a U-shaped quartz tube. The catalyst was reduced by 5% H_2/Ar at 400 °C for 30 min. After reduction, the sample was purged with pure He for 30 min and cooled down to 35 °C at 10 °C/min. Once the baseline was stable, CO chemisorption was performed, where 0.53 ml (STP) of 5% CO/He was injected into the He stream. The CO gas injection was repeated 30 times. A TCD signal vs. time plot was obtained and the Peak Editor software was used to estimate the area under the peaks in order to calculate the metal dispersion values.

2.3. EIS, UV-Vis DR, XPS and PL analyses

A Metrohm Autolab potentiostat/galvanostat PGSTAT302N equipped with an electrochemical impedance spectroscopy (EIS) FRA32M module was used to perform EIS measurements under Schott KL 1600 LED visible-light illumination in the frequency range of 0.1–10^6 Hz. To carry out the experiments in 0.1 M KOH electrolyte, a Metrohm DropSens Ramancell PTFE electrochemical cell was employed. The investigated materials were immobilized on the working electrode of the disposable Metrohm DropSens DRP-150 screen-printed carbon electrodes.

A Perkin-Elmer Lambda 35 UV-Vis spectrophotometer equipped with the RSA-PE-19 M Praying Mantis accessory for powdered samples was used to obtain the UV-Vis diffuse reflectance spectra of the prepared materials. The background correction was performed with the Spectralon© material.

The photoluminescence (PL) emission spectra of the prepared catalysts were recorded by means of a Perkin-Elmer LS-55 UV-Vis fluorescence spectrophotometer at the excitation wavelength of 315 nm.

X-Ray Photoelectron Spectroscopy analysis was performed using the Supra+ instrument (XPS, Kratos, Manchester, UK) equipped with an Al K_α excitation source and a monochromator. The powder samples were attached to double-sided tape, and the analyses were performed with an analysed spot size of 300 by 700 μm. The charge neutralizer was on during the analyses. High-resolution and survey spectra were measured with a pass energy of 20 and 160 eV, respectively. Spectra acquisition and data processing were performed using the ESCApe 1.4 software (Kratos, Manchester, UK).

2.4. Heterogeneous photocatalytic oxidation of an aqueous solution of bisphenol A

The photocatalytic degradation experiments of water-dissolved bisphenol A (Sigma-Aldrich, c_0(BPA)= 10.00 mg/l) under visible-light illumination (Philips 150 W halogen lamp) in the presence of the investigated materials ($c_{cat.}$=125 mg/l) were carried out at 25 °C and atmospheric pressure in a 250 ml Lenz Laborglas glass batch slurry reactor (model LF60). The bisphenol A/catalyst aqueous suspension was purged with 45 l/h of air and stirred at 600 rpm during the experiment. The so-called "dark" phase (30 min) was introduced before illumination with visible light to establish the sorption process equilibrium of bisphenol A onto the catalyst surface. An HPLC instrument (Thermo Scientific, model Spectra) was employed to monitor the degradation of bisphenol A as a function of the reaction/visible-light illumination time. For this purpose, a 100 × 4.6 mm BDS Hypersil C18 (2.4 μm) column was used and more details about the utilized HPLC analytical protocol can be found in our previous publication [38]. A total organic carbon analyser (Teledyne Tekmar, model Torch) was used to obtain data on the total organic carbon (TOC) content in fresh and treated BPA solutions with an observed measurement error within ± 1% for each of the three repetitions. A Perkin-Elmer 2400 Series II CHNS analyser was further used to determine the amount of carbon accumulated on the surface of the investigated catalysts during the BPA degradation runs.

2.5. H_2-assisted NO_2 photo and thermal catalytic reduction

The photo and thermal catalytic H_2-assisted NO_2 degradation reactions were conducted in a temperature-controlled Harrick Praying Mantis reaction chamber designed for Raman spectroscopy. The examined catalysts were aimed to be packed as thin as possible (4 mm, 20 mg), so that the maximum absorption of light was ensured. A Pfeiffer Vacuum Omnistar mass spectrometer was connected to the reaction chamber outlet for a quantitative real-time analysis of gaseous products. The catalyst samples were exposed to a gas mixture of 5000 ppm NO_2 and 5% H_2 in Ar with 70 ml/min gas flow. The samples were subsequently pre-treated in pure Ar for 60 min at 350 °C. Then the reactor was cooled down to 30 °C and exposed to the reaction mixture for 1 h for the conditioning and stabilization of the mass spectrometer. After that, the samples were gradually heated from 30° to 400°C with a 12 °C/min heating ramp.

The results from the thermal catalytic NO_2 reduction were further used to determine the temperature range for carrying out the photothermal catalytic NO_2 reduction. The catalyst samples were pre-treated in the same way as before in the thermal catalytic NO_2 degradation experiments. The photothermal catalytic NO_2 reduction runs were conducted in the temperature range of 50–200 °C with a temperature step of 25 °C. At each temperature step, the catalysts were initially in the dark for 15 min, so that the stabilization of the mass spectrometer response was established. After this, the samples were illuminated with a visible-light source for another 15 min. An OSRAM halogen lamp in 64657 HLX Newport 67011 arc lamp housing with a 69921 power supply, and a 1 m fibreglass light guide were used as a light source for the photocatalytic experiments.

3. Results and discussion

3.1. Characterization of photocatalysts

The size and morphology of the catalysts were assessed by SEM. Particulates in the a-TNR and TNR samples show a rod-like morphology with a diameter of ~10 nm and a length of 80–100 nm. In the TNP sample, we identified ellipsoidal TiO_2 particles with a length of 30 nm and a diameter of 20 nm (Fig. S1). The synthesis procedure of TiO_2 +Pt catalysts did not influence the morphology of the TiO_2 supports; the SEM-EDS chemical composition analysis of powders shows well-dispersed Pt particles (Fig. S2), and the actual loading of Pt is equal to the nominal one (SEM-EDS results are listed in Table S1).

The XRD diffractograms of the investigated materials illustrated in Fig. 1 show peaks that are typical for anatase TiO_2 (JCPDS 00–021–1272). In the XRD diffractogram of the bare a-TNR sample, the intensities of the peaks belonging to the anatase TiO_2 are very low, which can be ascribed to the amorphous TiO_2 shell covering the anatase core. In the XRD diffractograms of TNR and a-TNR+Pt samples, the intensities of anatase peaks are very strong, which provides evidence that the thermal treatment during the synthesis of TNR and a-TNR+Pt solids caused the crystallization of the amorphous TiO_2 shell in the a-TNR support into anatase phase. The average anatase crystallite size was calculated using the Scherrer formula from the width of the (001) diffraction peak (2θ=25°). The results listed in Table 1 show that the average anatase crystallite size in the bare TiO_2 supports is between 10 nm (a-TNR solid) and 19 nm (TNP and TNR samples), and that due to the thermal treatment during the synthesis procedure the anatase crystallite size in a-TNR+Pt catalyst increased to 17.4 nm. In the case of the TNR+Pt and TNP+Pt catalysts, the anatase crystallite size was not influenced by the deposition of Pt particles. The low intensity or absence of Pt diffraction peaks in the acquired XRD diffractograms of TiO_2 +Pt catalysts (Fig. 2) can be ascribed to the low amount of deposited Pt,

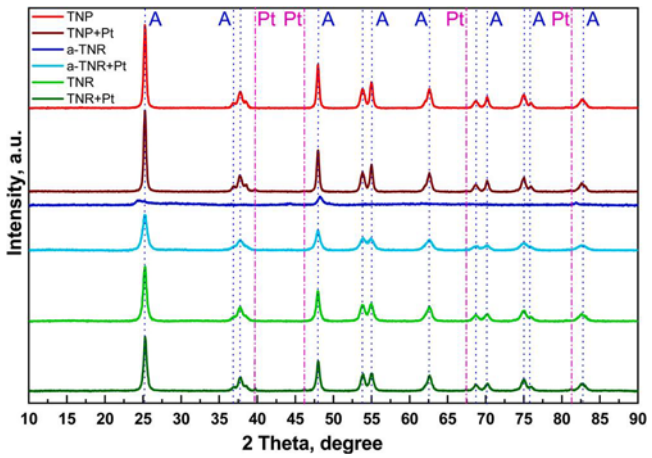

Fig. 1. XRD patterns of bare TiO_2 supports and synthesized TiO_2 +Pt catalysts. The vertical lines denote the standard data of anatase (blue, JCPDS no. 71–1167) and Pt (magenta, JCPDS no. 04–0802).

weak crystallinity, non-spherical shape and small size of the Pt particles, and/or the high dispersion of Pt particles over the TiO_2 supports [39–42]. The results of the XRD and TEM-SAED analysis show that in all the investigated samples, TiO_2 is only present in anatase form and that the calcination carried out at 300 and 500 °C did not result in the anatase-to-rutile transformation.

The representative samples were analysed by TEM; the particulates were directly visualized at different magnification scales, while their phase composition was analysed via selective-area electron diffraction (SAED) (Fig. 2). In the case of the TNP sample, the TiO_2 crystallites are near-spherical, with an average crystallite size of 17 nm (Std. dev. 5.5, min 6 nm, max 30 nm). For TNR samples, the TiO_2 particles are anisotropic with a similar diameter (~10–15 nm) while their length differs: a-TNR particles are shorter (~20 nm) while TNR particles appear longer (~100 nm). Although on the micron level, both TNR samples appear to have similar dimensions, we measured the size of the crystallites here and not only the size of the particles.

The TEM-selected area electron diffraction (SAED) patterns of the prepared TiO_2 +Pt catalysts (inset in Fig. 2, with ab-initio simulations for anatase, Pt, and their mixture) correspond to anatase TiO_2 and the minor presence of Pt in all the examined TiO_2 +Pt samples. The crystallite size of the Pt particles in the catalysts was measured from the TEM micrographs (Fig. 2) and the results are listed in Table 1. The particle size distribution of Pt particles in the TiO_2 +Pt catalysts in Fig. S3 show that the size of the Pt particles depends on the TiO_2 support employed. The size of Pt crystallites in TNR+Pt solid is ~2–3 nm, while for the TNP+Pt and a-TNR samples, the Pt crystallites appear larger and ~5–7 nm.

As shown by Žerjav et al. [18], the size of PM particles in the TiO_2 +PM catalysts can be influenced by the difference in the zeta potential value (pH_{PZC}) of TiO_2 supports. In this regard, we measured the zeta potential of the bare TiO_2 supports and the pH value of the aqueous Pt $(NH_3)_2(NO_2)_2$ solution used for the deposition of Pt particles. From the results presented in Fig. S4, we can see that the investigated TiO_2 supports can be divided into two groups based on the pH_{PZC} values. The pH_{PZC} values of the TNP and a-TNR samples are 2.8 and 3.5, and that of the TNR support equals 7.2, which means that the surfaces of the TNP and a-TNR supports are deprotonated during the wet impregnation procedure, and that of TNR support is protonated, because the pH value of the aqueous $Pt(NH_3)_2(NO_2)_2$ solution is 5.0. The negative charge of the TNP and a-TNR surfaces during the wet impregnation procedure positively influences the adsorption of the $Pt(NH_3)_2^{2+}$ complex [43,44] through a strong electrostatic attraction, compared to the positive charge of the TNR surface, and consequently larger Pt particles are formed in the case of TNP+Pt and a-TNR+Pt samples. We should further emphasize that the particle size distribution in the case of TNR+Pt catalyst was narrower than in the case of TNP and a-TNR supports (Fig. S3). In the case of TNP+Pt catalyst especially, a widespread Pt particle size distribution can be observed with smaller (below 2 nm) and larger (above 8 nm) Pt particles.

The diversity in the morphology of TiO_2 supports was also well expressed in the results of the N_2 physisorption analysis listed in Table 1. The corresponding N_2 adsorption-desorption isotherms and BJH pore size distributions are illustrated in Fig. S5. The specific surface areas (S_{BET}) of the bare TiO_2 supports are between 85.8 m^2/g (TNP) and 352 m^2/g (a-TNR). From our previous publications, we know that the a-TNR sample exhibits a core-shell structure consisting of an amorphous TiO_2 shell and anatase TiO_2 core, where upon the thermal treatment, the amorphous TiO_2 shell crystalizes into anatase TiO_2 [14]. The S_{BET} and pore volume (V_{pore}) values of the TNR and a-TNR+Pt samples decreased and the values of the pore diameter (d_{pore}) increased in comparison to the values of the a-TNR sample due to the crystallization of the amorphous TiO_2 shell, which leads to the elimination of micropores contained in the amorphous TiO_2 shell. The S_{BET}, V_{pore} and d_{pore} values of the TNP+Pt and TNR+Pt catalysts did not change significantly in comparison to the pure TiO_2 supports, which implies that the deposited Pt particles did not block the pores of the TiO_2 supports.

Fig. 3 presents the UV-Vis diffuse reflectance (UV-Vis DR) spectra and the corresponding Kubelka-Munk function of bare TiO_2 supports and prepared TiO_2 +Pt catalysts. The UV-Vis DR spectra of all the materials show a strong absorption in the wavelength range below 400 nm, which is given by the band gap of TiO_2 [17]. As can be seen in the UV-Vis DR spectra of the investigated TiO_2 +Pt catalysts, the introduction of Pt resulted in an increase of the absorption of light in the region between 400 and 800 nm, which is due to the plasmonic properties of the noble metal and the localized surface plasmon resonance (LSPR) [45]. The band gap values of the investigated solids obtained through the use of the Kubelka-Munk function are listed in Table 1. The absorption edge shift and the energy band change in the TiO_2 +Pt catalysts were only minor in comparison to the bare TiO_2 supports; this suggests that Pt is only deposited on the surface of the TiO_2 supports [42].

Another parameter that significantly influences the photocatalytic activity of a photocatalyst is the recombination rate of the light-

Table 1
Comparison of the specific surface area (S_{BET}), average pore diameter (d_{pore}), total pore volume (V_{pore}), anatase TiO_2 crystallite size at 25 °, band gap values of the investigated materials obtained with the Kubelka-Munk function, Schottky barrier height (SBH), charge transfer resistance (R_{CT}) and the dispersion of Pt particles.

Sample	S_{BET}	V_{pore}	d_{pore}	[a]TiO_2 crystallite size @ 25 °	Band gap	[b]SBH	R_{CT}	Pt dispersion
	m^2/g	cm^3/g	nm		eV		kΩ	%
TNP	85.8	0.29	13.7	19.0	3.30	/	138	/
TNP+Pt	63.6	0.26	15.7	19.0	3.20	0.41	9.8	13
a-TNR	352	0.96	8.9	10.4	3.40	/	399	/
a-TNR+Pt	149.1	0.63	16.9	17.4	3.25	0.38	17.4	25
TNR	105.0	0.57	19.3	19.0	3.30	/	309	/
TNR+Pt	85.1	0.44	20.0	19.0	3.25	0.50	30.9	26

[a] Calculated using the Scherrer formula and assuming that the TiO_2 particles are spherical.
[b] Calculated from the determined values of VBM in Fig. 6.

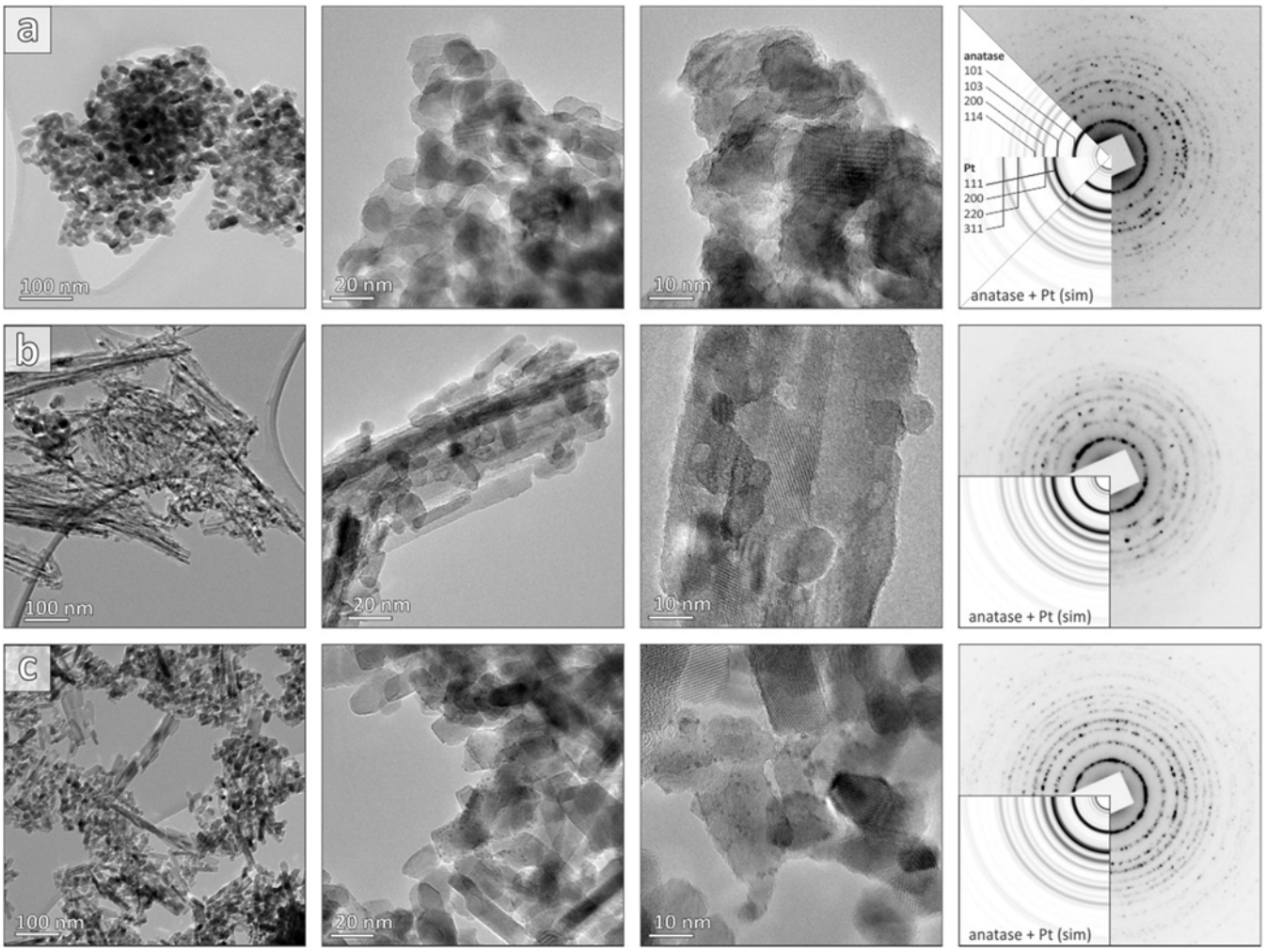

Fig. 2. TEM micrographs of the investigated TiO_2 +Pt catalysts obtained at different magnifications and TEM experimental selected area electron diffraction (SAED) patterns of prepared TiO_2 +Pt catalysts with simulated patterns of anatase TiO_2 and Pt ((a) TNP+Pt, (b) a-TNR+Pt, and (c) TNR+Pt samples).

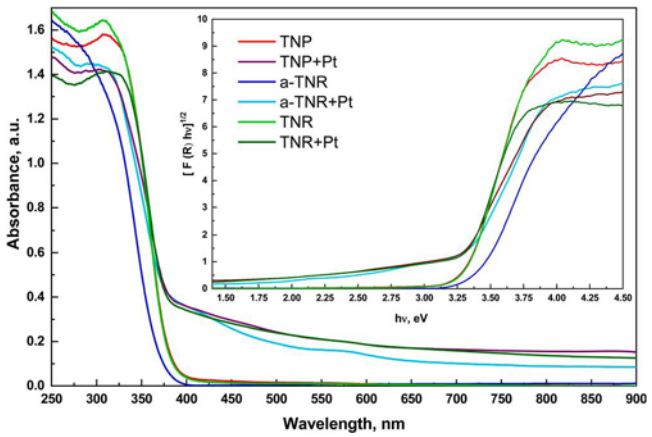

Fig. 3. UV-Vis-DR spectra of the bare TiO_2 supports and synthesized TiO_2 +Pt catalysts. The respective Kubelka-Munk function is present in the inset.

generated charge carriers, as a low charge carrier recombination rate is associated with high photocatalytic activity [45,46]. The photo-induced electrons and holes tend to recombine if they don't participate in any ROS generation reaction. With the recombination of charge carriers, energy in the form of photoluminescence (PL) emission is released; therefore, the intensity of the photoluminescence signal of a solid material is proportional to the electron-hole recombination rate. In the PL spectra of all the investigated materials displayed in Fig. 4, well-resolved shoulders/peaks were observed at around 3.2, 2.93, 2.7, 2.54 and 2.33 eV. Abazović et al. [47] ascribed the well-defined peak at 2.9 eV to the lowest indirect transition $\Gamma_{1b}\rightarrow X_{1a}$ and the signals at around 3.1 eV and above to direct ($X_{1b}\rightarrow X_{2b}$ at 3.59 eV and $X_{1b}\rightarrow X_{1a}$ at

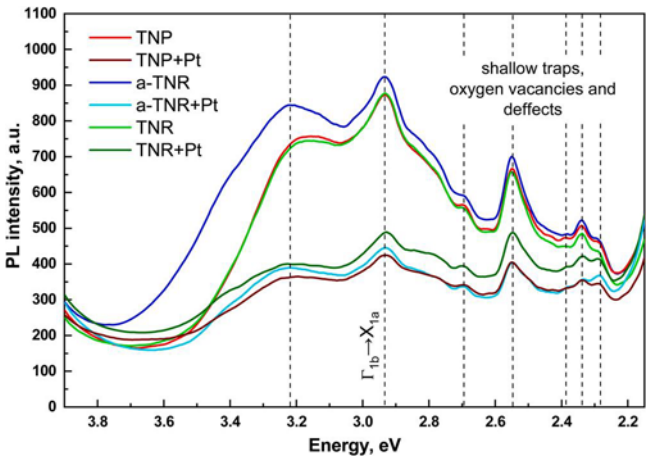

Fig. 4. Solid-state photoluminescence (PL) emission spectra of bare TiO_2 supports and synthesized TiO_2 +Pt catalysts.

3.45 eV) and indirect ($X_{1b}\rightarrow\Gamma_3$ at 3.19 eV and $\Gamma_{1b}\rightarrow X_{2b}$ at 3.05 eV) transitions in the anatase TiO_2. The peaks at 2.8, 2.7, 2.55 and 2.34 eV were further ascribed to the presence of the shallow traps. Kernazhitsky et al. [48], in their study of anatase and rutile TiO_2 solids, ascribed the strong excitonic peak at 2.91 eV to the recombination of self-trapped excitons, the peaks in the range between 2.71 and 2.80 eV to the excitonic recombination of charge carriers via oxygen vacancies, and the peaks at around 3.0 eV to indirect and direct transitions originating from the band-to-band charge carrier recombination. The origin of the decreased PL intensity in the case of the sample TNR, in comparison to the PL intensity of a-TNR solid (Fig. 4), lies in the calcination of the TNR sample at 500 °C and the growth of the anatase crystallite size from 10.4 to 19.0 nm (Fig. 2, Table 1) as the PL processes in solids are strongly affected by particle size, surface and bulk defects, calcination temperature, etc. This phenomenon was also observed by Liqiang et al. [49], who reported that the excitonic PL intensity of TiO_2 decreased due to the calcination of TiO_2 as a consequence of the particle size increase. The enhancement of the PL signal intensity in the PL solid-state spectra of different anatase TiO_2 samples was also observed by Kernazhitsky et al. [50] and attributed to the increase of the specific surface area and the associated increase of surface defect states, oxygen vacancies and the surface hydration degree of the investigated anatase TiO_2 samples. The PL solid-state spectra of the investigated TiO_2 +Pt catalysts in Fig. 4 exhibited lower PL signal intensities in comparison to the solid-state spectra of the bare TiO_2 supports regardless of the TiO_2 support employed. Nakajima et al. [51] attributed the decrease of the PL bands intensity of TiO_2 +Pt catalysts, in comparison to the PL band intensity of the pure TiO_2 supports, to differences in the work function between Pt and TiO_2 and not to differences in the specific surface area of the investigated materials. With the introduction of Pt particles onto the surface of TiO_2 supports, a junction is formed between the TiO_2 and Pt particles, which in turn enables the transport of light-generated "hot electrons" from Pt particles to the TiO_2 support. The role of the TiO_2 support in TiO_2 +Pt catalysts under visible-light illumination is to act as the sink for "hot electrons", thus prolonging the "lifetime" of the generated charge carriers. This is expressed as the decrease of the PL signal intensities in the PL solid-state spectra of the TiO_2 +Pt solids that can be observed in Fig. 4.

The electrochemical impedance spectroscopy (EIS) measurements were further employed to test the ability of the investigated photocatalysts in terms of the separation of visible-light-generated charge carriers. The electrochemical equivalent circuit (EEC) presented in Fig. S6 and composed of solution resistance (R_S), charge transfer resistance (R_{CT}), Warburg impendance (W), and the constant phase element (CPE), was used to fit the obtained Nyquist plots that are illustrated in Fig. 5. The R_{CT} values in the EEC are listed in Table 1 and indicate the charge transfer resistance at the electrode (photocatalyst)/electrolyte interface, with the diameter of the Nyquist's plot semicircle that reflects the charge transfer process [52]. The higher charge transfer resistance of a catalyst is expressed as the larger diameter of the semicircle [53–56]. It is not surprising that TiO_2 supports exhibit the highest R_{CT} values (between 138 and 399 kΩ) among the investigated materials. The highest R_{CT} value was obtained in the case of a-TNR sample, which also exhibited the highest BG value and the highest PL signal intensity (Fig. 4). The R_{CT} values of the TiO_2 +Pt catalysts were significantly lower than those of the TiO_2 supports and were in the range between 9.8 and 30.9 kΩ. The results of the EIS measurements show that the presence of Pt particles enables the TiO_2 +Pt catalysts to employ visible-light illumination to generate charge carriers, as was already postulated by the results of the UV-Vis DR spectra measurements (Fig. 3). The differences in the R_{CT} values of the TiO_2 supports originate in their different crystallite sizes, band gap energies and specific surface areas. The same can also be postulated for the TiO_2 +Pt catalysts, but here we also have to consider that at the junction between the TiO_2 support and Pt particles, an SB is formed. The height of the SB at the junction between TiO_2 and plasmonic metal can be influenced by the TiO_2 support [18] and the amount of added PM [17].

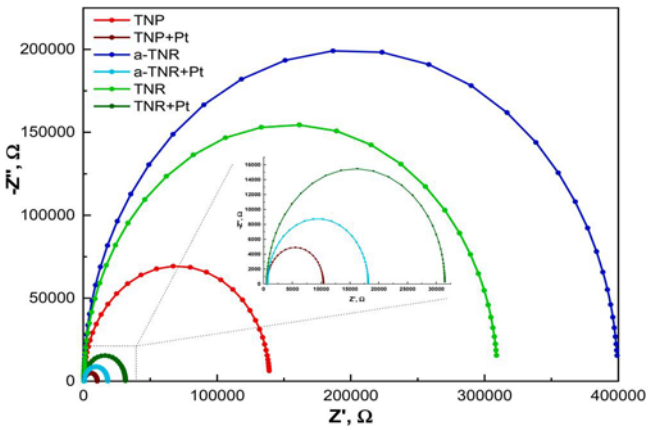

Fig. 5. EIS Nyquist plot of the bare TiO_2 supports and synthesized TiO_2 +Pt catalysts in a 0.1 M KOH electrolyte under visible-light irradiation. The dashed lines represent the data fitted with the electrochemical equivalent circuit presented in Fig. S6.

The results of the XPS analysis show that the Pt 4 f signal was detected for all the TiO_2 +Pt catalysts. The oxidation state of Pt was obtained by fitting the Pt 4 f spectra (Fig. S7). The position of the doublets (Pt 4 $f_{7/2}$ and Pt 4 $f_{5/2}$) corresponds to the Pt(II) and Pt(0) oxidation states for all three samples (quantitative results are given in Table S2) [57]. The shape and position of the Ti $2p_{3/2}$ and Ti $2p_{1/2}$ peaks were similar for all the samples apart from TNR+Pt (Fig. S8a). The latter sample shows a low-intensity shoulder on the high binding energy side, which suggests the presence of Ti(III), whereas the main Ti $2p_{3/2}$ peak corresponds to Ti(IV). The shape and position of the Ti 2p spectra for all the other samples suggest that the surface is composed of Ti(IV) species [58]. O 1 s spectra show three features (Fig. S8b). The feature located at dashed line 1 corresponds to the Ti suboxides and the charge transfer from Ti [59], and was expressed only for the TNR+Pt sample. The main peak for all the samples located at dashed line 2 originates from oxygen in the TiO_2. The feature at dashed line 3 corresponds to the oxidized carbonaceous species, which adsorbed onto the surface during sample preparation and transfer to the spectrometer [58].

The formation of the Schottky barrier (SB) at the junction between the TiO_2 support and PM particles is expressed by the shift of the valence band maxima (VBM) of the TiO_2 +PM catalysts toward lower binding energies in comparison to the VBM of the bare TiO_2 support [60,61]. Fig. S9 presents a scheme of the band gap diagram of the TiO_2 support/Pt particles system and schematically shows the formation of SBH and the transfer of visible-light-generated "hot electrons" from Pt particles to the TiO_2 support. The net charge transfer occurs continuously until the Fermi levels of both components are aligned [62]. Upon this, an electric field known as SBH ($\varnothing_{SB}$) is created at the TiO_2 support/Pt particles junction that results in the presence of a potential barrier for electrons moving from Pt particles to the TiO_2 support and is defined as [63]:

$$\varnothing_{SB} = \varnothing_M - \chi \quad (1)$$

The $\varnothing_{SB}$ in Eq. (1) presents the SBH between Pt particles and TiO_2 support, χ represents the electron affinity of TiO_2, and $\varnothing_M$ stands for a work function of Pt. The literature search reveals that the electron affinity of TiO_2 is in the range between 4.9 and 5.1 eV [64], and the $\varnothing_M$ equals to 5.6 eV [65]. The migration of electrons at the TiO_2/Pt interface is facilitated by lowering of the $\varnothing_{SB}$ value. The results of the VBM measurements of the investigated materials are illustrated in Fig. 6. The VBM positions of the measured materials with respect to the Fermi level (EF) were found to be 2.91, 3.25 and 2.84 eV for the TNP, a-TNR and TNR samples, respectively. Based on the results of the XPS measurements presented in Fig. 6, the VBM values of the catalysts shifted toward

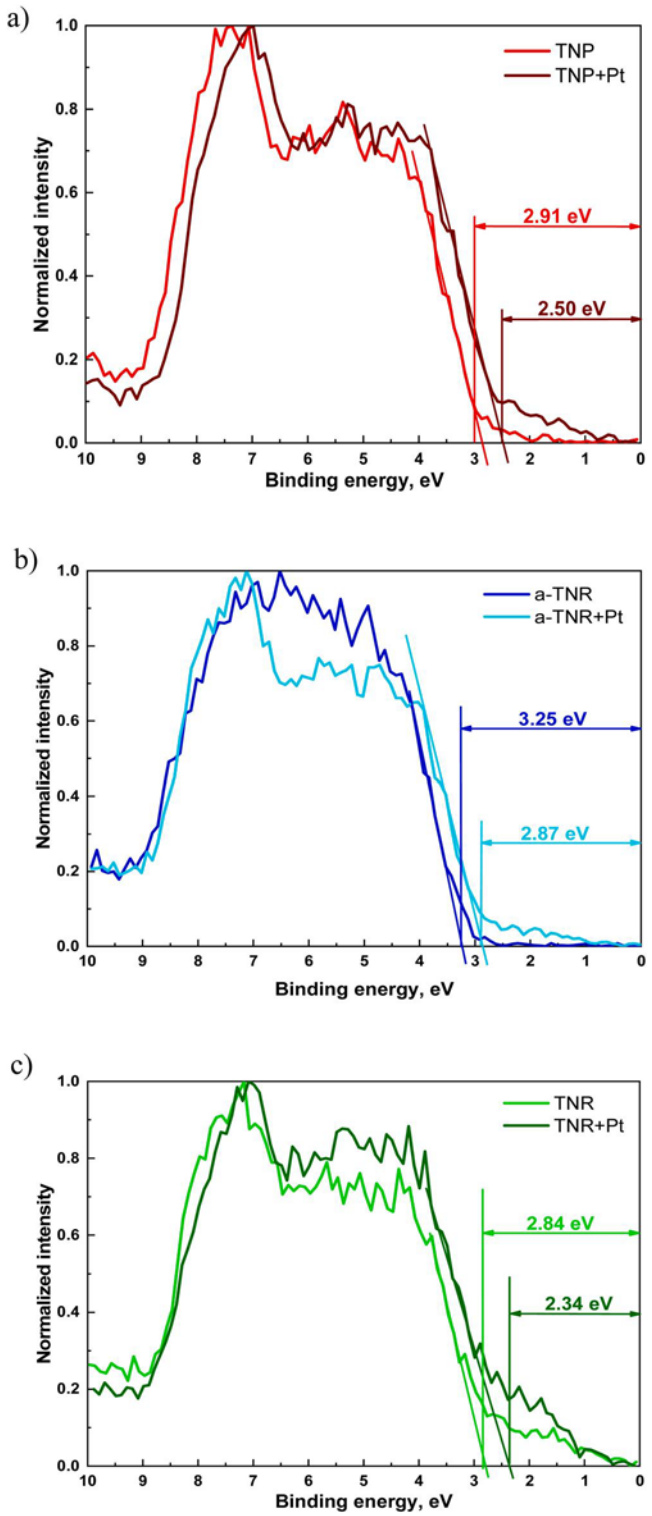

Fig. 6. Determination of the VBM of the bare TiO_2 supports and TiO_2 +Pt catalysts by means of XPS analysis.

lower binding energies in comparison to the VBM values of bare TiO_2, which means that the $\varnothing_{SB}$ values of the investigated a-TNR+Pt, TNR+Pt and TNP+Pt catalysts are 0.38, 0.50 and 0.41 eV, respectively. It was reported previously that the light-generated "hot electrons" in the PM have an energy of 1–2 eV [66–68], which is enough to overcome the SB in all of the investigated TiO_2 +Pt samples. The light-generated "hot electrons" in the TNR+Pt solid need to overcome a higher SB than the "hot electrons" in the a-TNR+Pt and TNP+Pt catalysts. This means that the "hot electrons" in the TNR+Pt catalyst need more time to overcome the SB. The consequence is that the "hot electrons" agglomerate at the SB and become more susceptible to recombination with the generated Pt holes and so less generated "hot electrons" can be transferred to the TNR support and be used, for example, for ROS generation. This is also in the agreement with the results of the solid-state PL measurements (Fig. 4).

The redox properties of the investigated TiO_2 +Pt samples were analysed by means of the H_2-TPR technique. Fig. 7 shows the obtained H_2-TPR profiles of the pre-oxidized TiO_2 +Pt samples. The low-temperature reduction peaks (below 150 °C) can be ascribed to the reduction of Pt oxides to metallic Pt [69–72]. The differences in the position of the low-temperature reduction peaks for the investigated TiO_2 +Pt catalysts can be attributed to differences in the formed Pt oxides (surface platinum oxide (Pt_sO), PtO and PtO_2), as well as differences in the particle size and crystallinity degree of the formed Pt oxides [73,74]. The results of the XPS Pt 4 f measurements listed in Table S2 reveal that the different ratios between the Pt(II) and Pt(0) oxidation states occur for the investigated TiO_2 +Pt catalysts. Depending on the TiO_2 support used, different amounts of metallic Pt and Pt oxides are thus formed on the catalyst surface exhibiting different reduction properties. Further, the results of the H_2-TPR analysis are in accordance with the results of the TEM analysis. In the latter, it was observed that the average particle size of Pt particles depends on the TiO_2 support used and that the smallest Pt particles (average size of ~2–3 nm, Fig. S3) and a narrow Pt particle size distribution were obtained in the case of the TNR+Pt sample. The latter solid exhibited the low-temperature reduction peaks at the lowest temperatures (−10, 30 and 100 °C) among the investigated TiO_2 +Pt catalysts due to the higher reducibility of small Pt particles. The particle size distribution of Pt particles in the case of the TNP+Pt sample (Fig. S3) shows a much broader distribution ranging from small to large Pt particles with an average size of ~5–7 nm. Due to this broadening of the particle size of the Pt particles, the TNP+Pt H_2-TPR profile exhibits reduction peaks in both the low-temperature range (0–90 °C) and at higher temperatures (350 °C). In the H_2-TPR profile belonging to the a-TNR+Pt sample, the reduction peak was observed at around 150 °C. The absence of reduction peaks at lower temperatures could be explained by the absence of small diameter Pt particles (below 2 nm), as was shown by the particle size distribution of Pt particles for the a-TNR+Pt sample in Fig. S3. It is well known that a partial reduction of TiO_2 by H_2 occurs at temperatures above 500 °C, therefore, the high-temperature reduction (above 300 °C) observed in the H_2-TPR profiles of the investigated TiO_2 +Pt samples could be attributed to the Pt-catalysed reduction of TiO_2 (spillover effect) [69, 75]. The literature search revealed that the differences in the

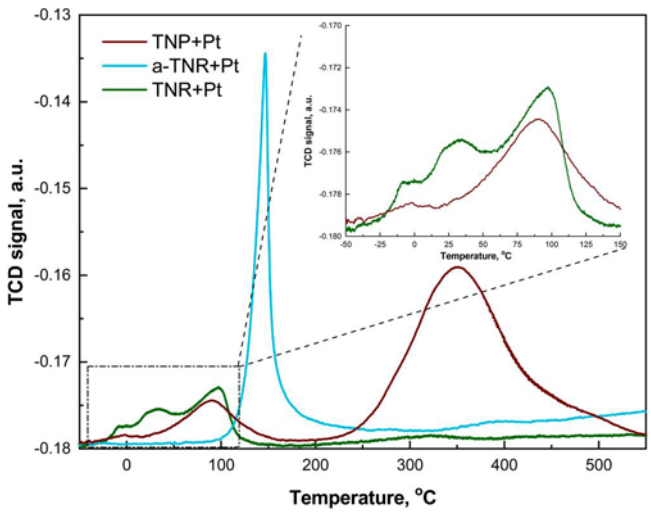

Fig. 7. H_2-TPR profiles of the investigated TiO_2 +Pt catalysts.

high-temperature H_2-TPR profiles of the examined solids can be ascribed to differences in the interaction of Pt oxides with the TiO_2 supports [76], different dispersion of Pt on the catalyst surface [77], and differences in the specific surface area and crystallinity of the TiO_2 supports [69]. The results of the characterizations performed on the investigated TiO_2 +Pt catalysts revealed that we deal with TiO_2 supports exhibiting different specific surface area and sizes of TiO_2 crystallites (Table 1), as well as different interactions between the TiO_2 supports and Pt particles (Fig. 6, Table 1). Further, the results of the CO chemisorption analysis listed in Table 1 demonstrate that the dispersion of Pt metallic particles depends on the employed TiO_2 support. The above-described differences in the redox properties of the synthesized TiO_2 +Pt catalysts will play a significant role in the H_2-assisted thermal catalytic decomposition of NO_x, as Liu et al. [76] already attributed the improved low-temperature reduction of NO_x carried out over a TiO_2/WO_3 +Pt catalyst in the presence of more reducible Pt oxides, in comparison to the TiO_2 +Pt catalyst. In addition, Nanba et al. [78] showed that the temperature window of the selective reduction of NO with H_2 in the presence of excess O_2 (the NO–H_2–O_2 reaction) over a Pt/Al_2O_3 catalyst is significantly affected by the nature of the Pt particles.

3.2. Catalytic activity

3.2.1. Photocatalytic oxidation of water-dissolved bisphenol A

The ability of the prepared TiO_2 +Pt materials to undergo the visible-light-triggered degradation of water-dissolved bisphenol A (BPA) was tested in a batch slurry reactor system. Preliminary experiments, the results of which are not included in this manuscript, confirmed that the photocatalytic oxidation runs were performed in the kinetic regime and therefore not influenced by mass-transfer resistances. The adsorption of BPA onto the surface of the investigated catalysts was tested during the so-called "dark" period (marked by the grey area in Fig. 8a) of 30 min. The adsorption of BPA onto the surface of bare TiO_2 supports and TiO_2 +Pt catalysts can be neglected, as the results in Fig. 8 show that the BPA concentration in the aqueous solution was constant during the "dark" period for all tested materials.

Pure TiO_2 supports showed a minor BPA degradation under visible-light illumination (between 17% and 25% after 120 min of visible-light irradiation), which was due to the presence of surface Ti^{3+} species or surface defects [79,80]. The addition of Pt onto the TiO_2 supports significantly enhanced the degradation of water-dissolved BPA. The highest photocatalytic activity involving BPA degradation under visible-light illumination was exhibited by the TNP+Pt sample, which showed complete BPA degradation already after 70 min of illumination, followed by the a-TNR+Pt solid that attained complete BPA degradation after 120 min of illumination. The lowest BPA degradation rate was obtained in the presence of the TNR+Pt catalyst, which degraded 80% of the initial BPA amount in 120 min under visible-light illumination.

To monitor the extent of BPA mineralization (i.e. the deep oxidative transformation to CO_2), TOC analysis of fresh and treated BPA solutions, as well as CHNS elemental analysis of fresh and spent catalysts were carried out (Table S3). This enabled us to determine the amount of accumulated BPA and/or BPA degradation products on the surface of the investigated materials (TOC_A). These results were further used to calculate the amount of real mineralization (TOC_M); the data is illustrated in Fig. 8b. One can see that pure TNP, with the lowest specific surface area of all the tested TiO_2 supports, tends to accumulate much less of the BPA degradation products than the bare TNR and a-TNR samples. By introducing Pt particles on the TiO_2 supports, the extent of the mineralization significantly increased. The order of the mineralization extent obtained in the series of TiO_2 +Pt catalysts is the same as the one concerning the BPA degradation rates. The TOC_A values reveal that the higher specific surface area can also have a detrimental effect on the photocatalytic activity of catalysts in heterogeneous photocatalysis for wastewater treatment. Namely, the results in Fig. 8b show that the a-TNR+Pt and TNR+Pt samples exhibit a higher affinity to adsorb BPA

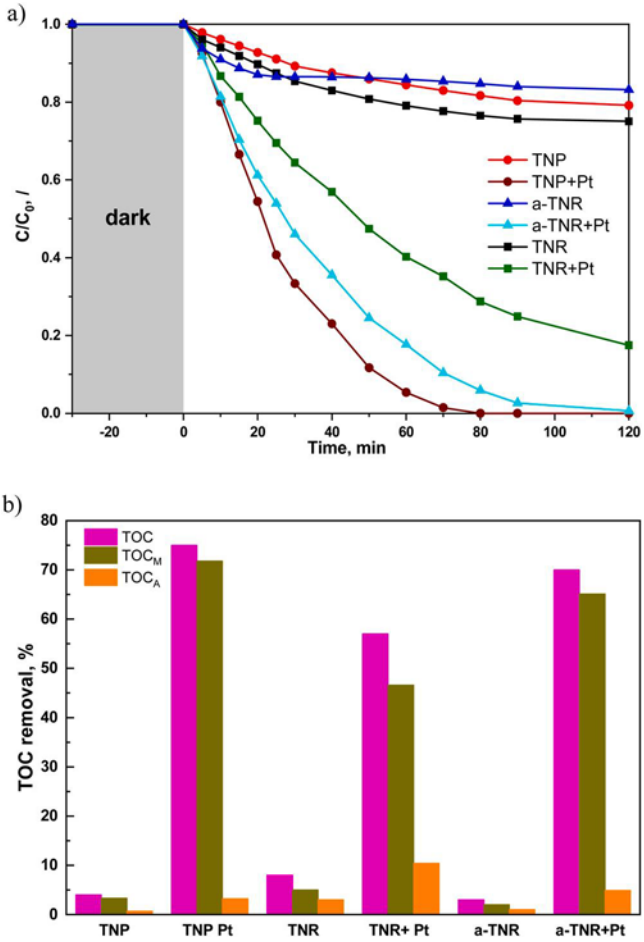

Fig. 8. (a) Photocatalytic degradation of an aqueous solution of BPA (c_0 =10.0 mg/l) conducted at T = 25 °C in the presence of bare TiO_2 supports and synthesized TiO_2 +Pt catalysts ($c_{cat.}$=125 mg/l) under visible-light illumination. (b) The reported values of total organic carbon (TOC) removal represent a sum of TOC mineralization (TOC_M) and TOC accumulation (TOC_A) measured at the end of the BPA degradation runs.

degradation products compared to the TNP+Pt catalyst. Due to this, the surfaces of the a-TNR+Pt and TNR+Pt samples get blocked and cannot participate in the formation of ROS by the generated charge carriers. In the case of a-TNR+Pt sample, the impact of the surface-blocking process on the BPA degradation, expressed at a later stage of the reaction course, is due to the almost 50% higher specific surface area. Another drawback of the TNR+Pt catalyst that decreases photocatalytic efficiency in comparison to the a-TNR+Pt and TNP+Pt samples, is its high SB, which prolongs the transfer time of the generated "hot electrons" into the TNR support and therefore makes them more susceptible to the charge carrier recombination process.

3.2.2. H_2-assisted thermal and photothermal reduction of NO_2

The temperature-dependent direct H_2-assisted NO_2 reduction in the temperature range between 30 and 400 °C was studied over bare TiO_2 supports and TiO_2 +Pt catalysts by monitoring the decrease of the NO_2 concentration (as ion current) in the flow-through (photo)catalytic reactor. The corresponding NO_2 conversions versus temperature dependencies, which are illustrated in Fig. 9a, were calculated based on the calibration curve shown in Fig. S10. In Fig. S11, one can see the results of a blank experiment performed using an empty reactor; they confirm that the reactor walls negligibly contribute to the disappearance of NO_2. The results in Fig. 9a show that bare TiO_2 supports exhibit no catalytic activity toward the degradation of NO_2 in the investigated

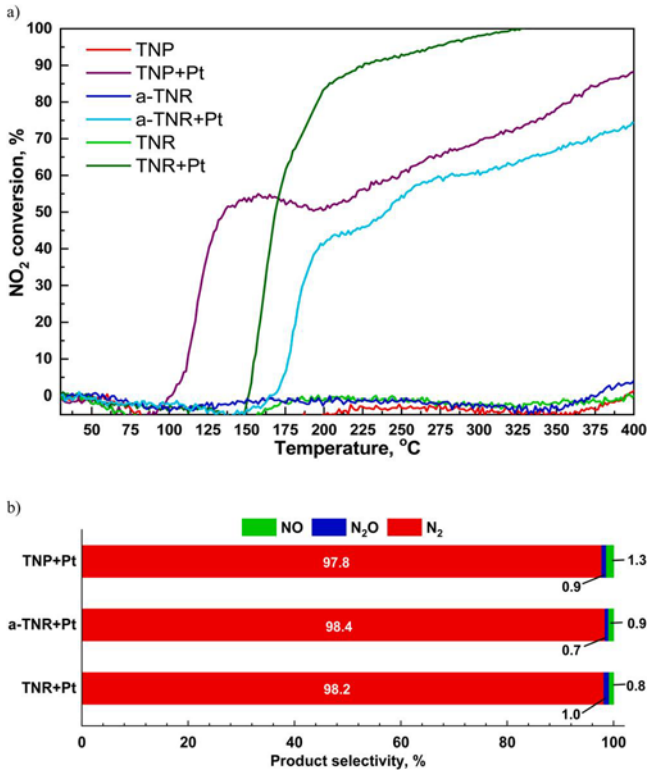

Fig. 9. (a) Temperature-dependent relative NO_2 conversion over bare TiO_2 supports and TiO_2 +Pt catalysts calculated based on the calibration curve present in Fig. S10. (b) Calculated relative percent selectivity of three major products (NO, N_2O and N_2) in the 30–400 °C temperature interval for the investigated TiO_2 +Pt catalysts.

temperature range. The addition of Pt onto TiO_2 supports enables the degradation of NO_2 in the investigated temperature interval, regardless of the employed TiO_2 support, although below 90 °C neither of the investigated TiO_2 +Pt catalysts exhibited any thermal catalytic activity. The lowest activity in the H_2-assisted deNO_2 process in the investigated temperature range was obtained in the presence of the a-TNR+Pt catalyst, while the TNR+Pt sample exhibited the highest activity. Another important aspect to be considered is product selectivity. During the NO_2 reduction using H_2, the three main products are NO, N_2O and N_2. The most desired product is N_2 due to its nontoxic characteristics, while NO and N_2O are major greenhouse and toxic gasses. Fig. S12 shows the MS ion current values for the three major detectable products as a function of increasing the reaction temperature from 30° to 400°C. The relative selectivity of the examined catalysts was calculated by integrating the area under ion current curves for each product [81] in the investigated temperature range. The results presented in Fig. 9b are promising, as they reveal that all the examined TiO_2 +Pt catalysts exhibit high selectivity toward N_2 formation (between 97.8% for the TNP+Pt sample and 98.4% for the a-TNR+Pt solid). Although the obtained selectivity values toward N_2 formation among the investigated samples differ only marginally, the difference in the ignition temperature of the H_2-assisted NO_2 reduction process is more significant. The TNP+Pt sample exhibited a reaction ignition temperature of 90 °C, the TNR+Pt sample of 150 °C, and the a-TNR+Pt sample of 159 °C. The differences in the temperature profiles of the NO_2 reduction process obtained by the investigated catalysts can be ascribed to the diversity in the reduction properties of the studied samples, which was observed in the H_2-TPR profiles illustrated in Fig. 7. We can conclude that the presence of easily reducible Pt oxides decreased the ignition temperature of the NO_2 reduction process, as already reported by other authors [76,78]. The decrease and increase of the NO_2 reduction rate exhibited by the TNP+Pt and a-TNR+Pt samples in the temperature region between 120 and 250 °C (Fig. 9a) can be ascribed to the Pt catalysed reduction of TiO_2.

Further, we investigated if we could lower the ignition temperature of the H_2 deNO_2 process by upgrading the thermal catalysis with photocatalysis. According to the observations of Christopher et al. [82], a decrease of the reaction temperature by 25 °C can increase the lifetime of a catalyst by about ten-fold. The TiO_2 +Pt catalysts were examined in the temperature range between 50 and 200 °C with temperature increments of 25 °C. The samples were first kept at the investigated temperature for 30 min, so that the MS ion current signal was stable. After this, we switched on the light source and waited for another 30 min to obtain a stable MS ion current signal; this was then repeated for each temperature increase. It should be noted that no increase of the temperature due to light illumination was detected by the temperature probe of the reaction chamber. However, we also note that this observation does not rule out a significant temperature increase at the sample position, since the temperature probe of the chamber is located a significant distance from the sample. We can see in Fig. 10 that the light illumination of the catalyst surface increased the extent of NO_2 conversion (here we also used the calibration curve presented in Fig. S10 to calculate the NO_2 conversion values). The highest additional benefit of photocatalysis in the photothermal NO_2 reduction was observed in the presence of the TNR+Pt catalyst. Although this catalyst exhibits the highest SBH, the highest photocatalytic activity of this sample in the NO_2 reduction process among the investigated TiO_2 +Pt catalysts can be ascribed to the second role of the SB at the junction between TiO_2 and PM, which is to prevent "hot electrons" being re-injected from the TiO_2 support to PM particles (Fig. S9). This leads to the accumulation of "hot electrons" in the conduction band of TiO_2, thus enabling them to achieve higher energy levels and increase their reduction potential [83]. In addition, we need to consider that the LSPR effect expressed by Pt particles can also affect the chemical process by heat generation via light absorption and coupling of "hot electrons" to the phonon bath (thermalization) and optical nearfield enhancement [84–86]. The processes can occur separately or side by side, making one of the key efforts in the field of plasmonic catalysis to find out how to distinguish between them [87,88]. Baffou et al. [89] proposed various simple experimental procedures to distinguish between the photothermal process and the "hot carrier" process in plasmonic catalysis, which avoid the use of thermal microscopy techniques. One of them is to plot the measured chemical reaction rate or any readout of the amount of reaction products as a function of the light source power, where a linear dependence under moderate light power and a super-linear dependence for very high light

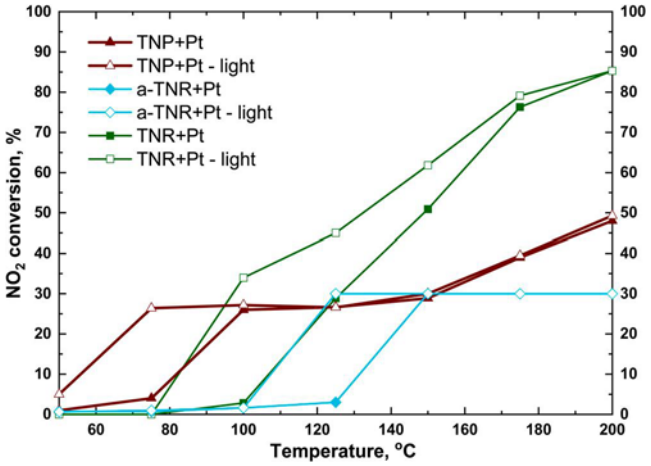

Fig. 10. NO_2 conversion versus temperature curves (solid symbols) and visible-light-assisted NO_2 conversion versus temperature curves (open symbols) over bare TiO_2 supports and TiO_2 +Pt catalysts.

power [90,91] would indicate a photochemical process and an exponential increase a photothermal effect [89]. We performed the photothermal degradation of NO_2 for the investigated samples at the lowest temperatures, at which we observed the highest beneficial influence of photocatalysis (i.e. 75 °C for the TNP+Pt sample, 125 °C for the a-TNR+Pt sample, and 100 °C for the TNR+Pt sample, Fig. 10) dependant on the increasing power of the light source (from 0 to 250 W). Fig. S13 shows the obtained curves of the increase of NO_2 conversion versus illumination light power. In the case of the TNP+Pt and a-TNR+ Pt samples, the trends of NO_2 conversion increase follow the linear dependence for moderate light power (dashed blue line in Fig. S13) and super-linear dependence (dashed green line in Fig. S13) for high light power. In the case of the TNR+Pt sample, NO_2 conversion follows the same linear fit regardless of the light power. The obtained experimental data for the a-TNR+Pt and TNR+Pt samples in Fig. S13 also show a good fit if an exponential function is used (dashed red line). The dilemma of whether the same experimental data could be fitted well with linear or exponential functions was also pointed out by Baffou et al. [89]. In practice, it is difficult to obtain an experimental data set that is large enough to be satisfactorily fitted with either exponential or linear functions, as this would mean extremely sensitive measurements of reaction rates at low or very high light powers would be required [89]. We can tentatively conclude that the "nature" of the LSPR effect in the investigated TiO_2 +Pt catalysts differs due to the use of various TiO_2 supports. The purpose of the above discussion was to draw attention to the various influences of the Pt LSPR effect on the chemical process, and to point out that more effort should be devoted to researching this phenomenon in the future. However, the obtained results of the H_2-assisted NO_2 reduction confirm that the investigated TiO_2 +Pt catalysts function as photo and thermal catalysts and can be used as catalysts in hybrid photothermal reaction systems.

Finally, the results of this study reveal that the role of SBH on the catalytic activity of the investigated TiO_2 +Pt photocatalysts depends on the nature of the application used. In the case of the heterogeneous photocatalytic oxidation of aqueous BPA solution, the photocatalytic activity of the investigated TiO_2 +Pt catalysts increases with decreasing SBH, which means that the injection of "hot electrons" into TiO_2 CB has a major impact on the overall photocatalytic BPA degradation efficiency due to the high demand for the "hot electrons" at the TiO_2/liquid interface to participate in the oxygen reduction process to generate ROS (i.e. superoxide anion radicals). Obviously, in the given range of reaction and operating conditions, the concentration of water-dissolved oxygen was sufficiently high not to limit the extent of oxygen surface reduction. On the contrary, in the case of the H_2-assisted $deNO_x$ reduction process, the participation of "hot electrons" in the reduction steps on the TiO_2 surface was not fast, which in turn favoured the reinjection of "hot electrons" from the TiO_2 support to Pt particles. Consequently, a high SBH (like in the TNR+Pt sample) was beneficial to enhance accumulation of "hot electrons" in the TiO_2 CB, allowing them to reach higher energy levels and increasing their reduction potential [83]. However, this remains to be investigated by, for example, conducting the H_2-assisted $deNO_x$ reduction process at higher concentrations of NO_2 in the gas phase.

4. Conclusions

The wet impregnation technique was used to synthesize TiO_2 +Pt catalysts with 1 wt% Pt loading and three different TiO_2 supports, which differ in the specific surface area and the morphology (anatase nanoparticles (TNP, S_{BET}(TNP)= 85 m^2/g), polycrystalline nanorods (a-TNR, S_{BET}(a-TNR)= 352 m^2/g) and single-crystal anatase nanorods (TNR, S_{BET}(TNR)= 105 m^2/g)). The results of TEM and H_2-TPR analyses show that, based on the nature of the TiO_2 support, different average Pt particle sizes and the Pt particle size distribution, species of Pt oxides with different sizes, crystallinities and degrees of interaction with the TiO_2 supports were formed during the wet impregnation procedure. The negatively charged TNP and a-TNR surfaces strongly attracted the positively charged $Pt(NH_3)_2^{2+}$ complex, which resulted in the formation of larger Pt particles (~5–7 nm), in contrast to the positively charged TNR surface where smaller Pt particles (~2–3 nm) were formed. The UV-Vis DR spectra of the investigated solids revealed that the catalysts exhibited the ability to generate charge carriers under visible-light illumination due to the formation of SB, which enabled the separation of charge carriers and the prolongation of their "life" time by transferring the visible-light-generated Pt "hot electrons" to the TiO_2 supports. The SBH in the a-TNR+Pt, TNR+Pt and TNP+Pt samples were obtained by means of XPS analysis and found to be 0.38, 0.50 and 0.41 eV, respectively.

The low-visible-light-triggered photocatalytic activity of the TNR+Pt catalyst involving the oxidation of water-dissolved BPA is attributed to its high SBH and affinity to adsorb BPA and/or BPA degradation products, which means that the generation of ROS during the liquid-phase BPA oxidation process is hindered. The results of the thermal catalytic H_2-assisted NO_2 degradation performed over the TiO_2 +Pt catalysts in the temperature range of 30–400 °C showed that differences in the temperature profiles of the NO_2 reduction process occurred due to the diversity in the reduction properties of the studied solids. The TNP+Pt catalyst exhibited the lowest ignition temperature in the NO_2 reduction due to the presence of easily reducible Pt oxides. In the case of a-TNR+Pt and TNP+Pt catalysts, a decrease in the NO_2 reduction rate was observed in the temperature range of 120–250 °C as a consequence of the Pt catalysed reduction of TiO_2 supports. All the investigated TiO_2 +Pt catalysts exhibited a high selectivity toward N_2 formation of over 97%. In addition, visible-light illumination of TiO_2 +Pt catalysts at temperatures below 200 °C beneficially increased the NO_2 conversion and lowered the ignition temperature of the $deNO_x$ process due to the Pt LSPR effect. The highest catalytic activity involving the H_2-assisted NO_2 reduction observed for the TNR+Pt catalyst can be ascribed to the presence of a narrow particle size distribution of small Pt particles, the absence of the Pt catalysed reduction of the TNR support at higher temperatures, and the beneficial effect of a higher SBH to prevent the reinjection of "hot electrons" from the conduction band of TNR to Pt particles. One should also not forget that the LSPR effect of the Pt particles can affect the NO_x decomposition by the photothermal heat production process.

The results of this study show that the prepared TiO_2 +Pt plasmonic catalysts can be used as photo, thermal and photothermal catalysts in both gas-solid and gas-liquid-solid environmental applications, and that the catalytic performance of the examined solids depends on their morphological, optical and electronic properties, as well as on the properties/conditions of the application in which they are used as catalysts.

CRediT authorship contribution statement

Gregor Žerjav: Conceptualization, Investigation, Validation, Writing – original draft, Visualization, Supervision. **Zafer Say:** Investigation, Writing – review & editing. **Janez Zavašnik**: Investigation, Visualization. **Matjaž Finšgar:** Investigation, Visualization. **Christoph Langhammer:** Writing – review & editing. **Albin Pintar:** Investigation, Writing – review & editing, Funding acquisition.

Declaration of Competing Interest

The authors declare that they have no known competing financial interests or personal relationships that could have appeared to influence the work reported in this paper.

Data Availability

Data will be made available on request.

Acknowledgements

The authors acknowledge the financial support from the Slovenian Research Agency (research core funding nos. P2-0150, P1-0417, P2-0118). The project is co-financed by the Republic of Slovenia, the Ministry of Education, Science and Sport and the European Union under the European Regional Development Fund.

Appendix A. Supporting information

Supplementary data associated with this article can be found in the online version at doi:10.1016/j.jece.2023.110209.

References

[1] J.J. Rueda-Marquez, I. Levchuk, P.F. Ibañez, M. Sillanpää, A critical review on application of photocatalysis for toxicity reduction of real wastewaters, J. Clean. Prod. (2020), 120694.
[2] U.G. Akpan, B.H. Hameed, Photocatalytic degradation of 2,4-dichlorophenoxy-acetic acid by Ca-Ce-W-TiO_2 composite photocatalyst, Chem. Eng. J. 173 (2011) 369–375.
[3] L. Lin, R.-H. Li, Y. Li, J. Xu, X.-Y. Li, Recovery of organic carbon and phosphorus from wastewater by Fe-enhanced primary sedimentation and sludge fermentation, Process Biochem. 54 (2017) 135–139.
[4] R. Mustafa, E. Asmatulu, Preparation of activated carbon using fruit, paper and clothing wastes for wastewater treatment, J. Water Process Eng. 35 (2020), 101239.
[5] X. Yang, Z. Wang, L. Shao, Construction of oil-unidirectional membrane for integrated oil collection with lossless transportation and oil-in-water emulsion purification, J. Membr. Sci. 549 (2018) 67–74.
[6] M. Sgroi, S.A. Snyder, P. Roccaro, Comparison of AOPs at pilot scale: energy costs for micro-pollutants oxidation, disinfection by-products formation and pathogens inactivation, Chemosphere (2020), 128527.
[7] J.S. George, A. Ramos, H.J. Shipley, Tanning facility wastewater treatment: analysis of physical–chemical and reverse osmosis methods, J. Environ. Chem. Eng. 3 (2015) 969–976.
[8] A.M. Chávez, O. Gimeno, A. Rey, G. Pliego, A.L. Oropesa, P.M. Álvarez, F. J. Beltrán, Treatment of highly polluted industrial wastewater by means of sequential aerobic biological oxidation-ozone based AOPs, Chem. Eng. J. 361 (2019) 89–98.
[9] C. Amor, J. Rodríguez-Chueca, J.L. Fernandes, J.R. Domínguez, M.S. Lucas, J. A. Peres, Winery wastewater treatment by sulphate radical based-advanced oxidation processes (SR-AOP): thermally vs UV-assisted persulphate activation, Process Saf. Environ. Prot. 122 (2019) 94–101.
[10] D.B. Miklos, W.L. Wang, K.G. Linden, J.E. Drewes, U. Hübner, Comparison of UV-AOPs (UV/H_2O_2, UV/PDS and UV/Chlorine) for TOC removal from municipal wastewater effluent and optical surrogate model evaluation, Chem. Eng. J. 362 (2019) 537–547.
[11] Q. Guo,C. Zhou, Z. Ma, X. Yang, Fundamentals of TiO_2 photocatalysis: concepts, mechanisms, and challenges, Adv. Mater. 31 (2019) 1901997.
[12] M. Roškarič, G. Žerjav, J. Zavašnik, A. Pintar, The influence of synthesis conditions on the visible-light triggered photocatalytic activity of g- C_3N_4/TiO_2 composites used in AOPs, J. Environ. Chem. Eng. 10 (2022) 1–17.
[13] G. Žerjav, J. Teržan, P. Djinović, Z. Barbieriková, T. Hajdu, V. Brezová, J. Zavašnik, J. Kovač, A. Pintar, TiO_2-β-Bi_2O_3 junction as a leverage for the visible-light activity of TiO_2 based catalyst used for environmental applications, Catal. Today 361 (2021) 165–175.
[14] G. Žerjav, M.S. Arshad, P. Djinović, J. Zavašnik, A. Pintar, Electron trapping energy states of TiO_2-WO_3 composites and their influence on photocatalytic degradation of bisphenol, Appl. Catal. B: Environ. 209 (2017) 273–284.
[15] G. Žerjav, G. Scandura, C. Garlisi, G. Palmisano, A. Pintar, Sputtered vs. sol-gel TiO_2-doped films: characterization and assessment of aqueous bisphenol A oxidation under UV and visible light radiation, Catal. Today 357 (2020) 380–391.
[16] M. Krbal, H. Sopha, V. Podzemna, S. Das, J. Prikryl, J.M. Macak, TiO_2 nanotube/chalcogenide-based photoelectrochemical cell: nanotube diameter dependence study, J. Phys. Chem., C. 121 (2017) 6065–6071.
[17] G. Žerjav, M. Roškarič, J. Zavašnik, J. Kovač, A. Pintar, Effect of Au loading on Schottky barrier height in TiO_2 + Au plasmonic photocatalysts, Appl. Surf. Sci. 579 (2022), 152196.
[18] G. Žerjav, J. Zavašnik, J. Kovač, A. Pintar, The influence of Schottky barrier height onto visible-light triggered photocatalytic activity of TiO_2+Au composites, Appl. Surf. Sci. 543 (2021) 14879.
[19] P. Wang, B. Huang, Y. Daia, M.-H. Whangbo, Plasmonic photocatalysts: harvesting visible light with noble metal nanoparticles, Phys. Chem. Chem. Phys. 14 (2012) 9813–9825.
[20] J. Gosciniak, F.B. Atar, B. Corbett, M. Rasras, Plasmonic Schottky photodetector with metal stripe embedded into semiconductor and with a CMOS-compatible titanium nitride, Sci. Rep. 9 (2019) 6048.
[21] G. McCarron, Air Pollution and human health hazards: a compilation of air toxins acknowledged by the gas industry in Queensland's Darling Downs, Int. J. Environ. Stud. 75 (2018) 171–185.
[22] P.E. Morrow, Toxicological data on NO_x: an overview, J. Toxicol. Environ. Health 13 (1984) 205–227.
[23] F. Normann, K. Andersson, B. Leckner, F. Johnsson, Emission control of nitrogen oxides in the oxy-fuel process, Prog. Energy Combust. Sci. 35 (2009) 385–397.
[24] S. Roy, M.S. Hegde, G. Madras, Catalysis for NO_x abatement, Appl. Energy 86 (2009) 2283–2297.
[25] V.I. Pârvulescu, P. Grange, B. Delmon, Catalytic removal of NO, Catal. Today 46 (1998) 233–316.
[26] P.S. Kim, M.K. Kim, B.K. Cho, I.-S. Nam, S.H. Oh, Effect of H_2 on deNO_x performance of HC-SCR over Ag/Al_2O_3: Morphological, chemical, and kinetic changes, J. Catal. 301 (2013) 65–76.
[27] N. Usberti, M. Jablonska, M.D. Blasi, P. Forzatti, L. Lietti, A. Beretta, Design of a "high-efficiency" NH_3-SCR reactor for stationary applications. A kinetic study of NH_3 oxidation and NH_3-SCR over V-based catalysts, Appl. Catal. B 179 (2015) 185–195.
[28] P.M. More, D.L. Nguyen, Activation by pretreatment of Ag–Au/Al_2O_3 bimetallic catalyst to improve low temperature HC-SCR of NO_x for lean burn engine exhaust, Appl. Catal. B 174–175 (2015) 145–156.
[29] C. Hahn, Matthias Endisch, F.J.P. Schott, S. Kureti, Kinetic modelling of the NO_x reduction by H_2 on Pt/WO_3/ZrO_2 catalyst in excess of O_2, Appl. Catal. B 168–169 (2015) 429–440.
[30] C.N. Cost, A.M. Efstathiou, Mechanistic aspects of the H_2-SCR of NO on a novel Pt/MgO-CeO_2, catalyst, J. Phys. Chem. C. 111 (2007) 3010–3020.
[31] C.N. Costa, P.G. Savva, J.L.G. Fierro, A.M. Efstathiou, Industrial H_2-SCR of NO on a novel Pt/MgO-CeO_2 catalyst, Appl. Catal. B 75 (2007) 147–156.
[32] L. Li, P. Wua, Q. Yu, G. Wu, N. Guan, Low temperature H_2-SCR over platinum catalysts supported on Ti-containing MCM-41, Appl. Catal. B 94 (2010) 254–262.
[33] Z. Liu, Y. Lu, L. Yuan, L. Ma, L. Zheng, J. Zhang, T. Hu, Selective catalytic reduction of NO_x with H_2 over WO_3 promoted Pt/TiO_2 catalyst, Appl. Catal. B 188 (2016) 189–197.
[34] V. Nair, M.J. Muñoz-Batista, M. Fernández-García, R. Luque, J.C. Colmenares, Thermo-photocatalysis: environmental and energy applications, ChemSusChem 12 (2019) 2098–2116.
[35] Y. Zhou, D.E. Doronkin, Z. Zhao, P.N. Plessow, J. Jelic, B. Detlefs, T. Pruessmann, F. Studt, J.-D. Grunwaldt, Photothermal catalysis over nonplasmonic Pt/TiO_2 studied by operando HERFD-XANES, resonant XES, and DRIFTS, ACS Catal. 8 (2018) 11398–11406.
[36] M. Ghoussoub, M. Xia, P.N. Duchesne, D. Segal, G. Ozin, Principles of photothermal gas-phase heterogeneous CO_2 catalysis, Energy Environ. Sci. 12 (2019) 1122–1142.
[37] K. Vikrant, C.M. Park, K.-H. Kim, S. Kumar, E.-C. Jeon, Recent advancements in photocatalyst-based platforms for the destruction of gaseous benzene: Performance evaluation of different modes of photocatalytic operations and against adsorption techniques, J. Photochem. Photobiol. C. 41 (2019), 100316.
[38] B. Erjavec, P. Hudoklin, K. Perc, T. Tišler, M. Sollner Dolenc, A. Pintar, Glass fiber-supported TiO_2 photocatalyst: efficient mineralization and removal of toxicity/estrogenicity of bisphenol A and its analogs, Appl. Catal. B 183 (2016) 149–158.
[39] D. Shi, J. Liu, S. Ji, Preparation of Au/TiO_2 catalyst and the performance of liquid methanol catalytic oxidation to formic acid, Ind. Eng. Chem. Res. 56 (2017) 11028–11033.
[40] M. Alvaro, B. Cojocaru, A.A. Ismail, N. Petrea, B. Ferrer, F.A. Harraz, V. I. Parvulescu, H. Garcia, Visible-light photocatalytic activity of gold nanoparticles supported on template-synthesized mesoporous titania for the decontamination of the chemical warfare agent Soman, Appl. Catal. B 99 (2010) 191–197.
[41] M. Mrowetz, A. Villa, L. Prati, E. Selli, Effects of Au nanoparticles on TiO_2 in the photocatalytic degradation of an azo dye, Gold. Bull. 40 (2007) 154–160.
[42] Y. Shu, J. Ji, M. Zhou, Shimin Liang, Q. Xie, S. Li, B. Liu, J. Deng, J. Cao, S. Liu, H. Huang, Selective photocatalytic oxidation of gaseous ammonia at ppb level over Pt and F modified TiO2, Appl. Catal. B 300 (2022), 120688.
[43] J.T. Miller, M. Schreier, A.J. Kropf, J.R. Regalbuto, A fundamental study of platinum tetraamine impregnation of silica: 2. The effect of method of preparation, loading, and calcination temperature on (reduced) particle size, J. Catal. 225 (2004) 203–212.
[44] C. Jiang, K. Hara, K. Namba, H. Kobayashi, S. Ittisanronnachai, H. Nishihara, T. Kyotani, A. Fukuoka, Preparation of highly dispersed Pt nanoparticles supported on zeolite-templated carbon and catalytic application in hydrogenation reaction, Chem. Lett. 43 (2014) 1794–1796.
[45] J.G. Yu, J.F. Xiong, B. Cheng, S.W. Liu, Fabrication and characterization of Ag-TiO_2 multiphase nanocomposite thin films with enhanced photocatalytic activity, Appl. Catal. B 60 (2005) 211–221.
[46] B. Cheng, Y. Le, J.G. Yu, Preparation and enhanced photocatalytic activity of Ag@TiO2 core–shell nanocomposite nanowires, J. Hazard. Mater. 177 (2010) 971–977.
[47] N.D. Abazović, M.I. Čomor, M.D. Dramićanin, D.J. Jovanović, S.P. Ahrenkiel, J. M. Nedeljković, Photoluminescence of anatase and rutile TiO_2 particles, J. Phys. Chem. B 110 (2006) 25366–25370.
[48] L. Kernazhitsky, V. Shymanovska, T. Gavrilko, V. Naumov, L. Fedorenko, V. Kshnyakin, J. Baran, Room temperature photoluminescence of anatase and rutile TiO_2 powders, J. Lumin. 146 (2014) 199–204.
[49] J. Liqiang, Q. Yichun, W. Baiqi, L. Shudan, J. Baojiang, Y. Libin, F. Wei, F. Honggang, S. Jiazhong, Review of photoluminescence performance of nano-sized semiconductor materials and its relationships with photocatalytic activity, Sol. Energy Mater. Sol. Cells 90 (2006) 1773–1787.
[50] L. Kernazhitsky, V. Shymanovska, T. Gavrilko, V. Naumov, L. Fedorenko, V. Kshnyakin, J. Baran, Room temperature photoluminescence of anatase and rutile TiO_2 powders, J. Lumin. 146 (2014) 199–204.

[51] H. Nakajima, T. Mori, Photoluminescence of Pt-loaded TiO2 powder, Phys. B 376–377 (2006) 820–822.

[52] S. Bhardwaj, A. Pal, K. Chatterjee, T.H. Rana, G. Bhattacharya, S.S. Roy, P. Chowdhury, G.D. Sharma, S. Biswas, Significant enhancement of power conversion efficiency of dye-sensitized solar cells by the incorporation of TiO_2-Au nanocomposite in TiO_2 photoanode, J. Mater. Sci. 53 (2018) 8460–8473.

[53] N. Li, G. Liu, C. Chen, F. Li, L. Zhang, H. Cheng, Battery performance and photocatalytic activity of mesoporous anatase TiO_2 nanospheres/graphene composites by template-free self-assembly, M. Adv. Funct. Mater. 21 (2011) 1717–1722.

[54] A. Jana, C. Bhattacharya, J. Datta, Enhanced photoelectrochemical activity of electro-synthesized CdS-Bi_2S_3 composite films grown with self-designed cross-linked structure, Electrochim. Acta 55 (2010) 6553–6562.

[55] Y. Chen, Y. Wang, W. Li, Q. Yang, Q. Hou, L. Wei, L. Liu, F. Huang, M. Ju, Enhancement of photocatalytic performance with the use of noble-metal-decorated TiO_2 nanocrystals as highly active catalysts for aerobic oxidation under visible-light irradiation, Appl. Catal. B 210 (2017) 352–367.

[56] Y. Zhang, N. Zhang, Z.-R. Wang, Y.-J. Xu, A unique silk mat-like structured Pd/CeO_2 as an efficient visible light photocatalyst for green organic transformation in water, ACS Sustain. Chem. Eng. 1 (2013) 1258–1266.

[57] Y. Su, Y. Deng, Effect of structure on the photocatalytic activity of Pt-doped TiO_2 nanotubes, Appl. Surf. Sci. 257 (2011) 9791–9795.

[58] M.C. Biesinger, L.W.M. Lau, A.R. Gerson, R.S.C. Smart, Resolving surface chemical states in XPS analysis of first row transition metals, oxides and hydroxides: Sc, Ti, V, Cu and Zn, Appl. Surf. Sci. 257 (2010) 887–898.

[59] V.D. Chinh, A. Broggi, L. Di Palma, M. Scarsella, G. Speranza, G. Vilardi, P. N. Thang, XPS spectra analysis of Ti^{2+}, Ti^{3+} ions and dye photodegradation evaluation of titania-silica mixed oxide nanoparticles, J. Electron. Mater. 47 (2018) 2215–2224.

[60] Z. Zhang, J.T. Yates, Band bending in semiconductors: chemical and physical consequences at surfaces and interfaces, Chem. Rev. 112 (2012) 5520–5551.

[61] M.S. Arshad, Š. Trafela, K. Žužek Rožman, J. Kovač, P. Djinović, A. Pintar, Determination of Schottky barrier height and enhanced photoelectron generation in novel plasmonic immobilized multisegmented (Au/TiO_2) nanorod arrays (NRAs) suitable for solar energy conversion applications, J. Mater. Chem. C. 5 (2017) 10509–10516.

[62] Z. Zhang, J.T. Yates, Band bending in semiconductors: chemical and physical consequences at surfaces and interfaces, Chem. Rev. 112 (2012) 5520–5551.

[63] R.T. Tung, The physics and chemistry of the Schottky barrier height, Appl. Phys. Rev. 1 (2014), 011304.

[64] D.O. Scanlon, C.W. Dunnill, J. Buckeridge, S.A. Shevlin, A.J. Logsdail, S. M. Woodley, C.R.A. Catlow, M.J. Powell, R.G. Palgrave, I.P. Parkin, G.W. Watson, T.W. Keal, P. Sherwood, A. Walsh, A.A. Sokol, Band alignment of rutile and anatase TiO_2, Nat. Mater. 12 (2013) 798–801.

[65] B. Ofuonye, J. Lee, M. Yan, C. Sun, J.-M. Zuo, I. Adesida, Electrical and microstructural properties of thermally annealed Ni/Au and Ni/Pt/Au Schottky contacts on AlGaN/GaN heterostructures, Semicond. Sci. Technol. 29 (2014), 095005.

[66] S.M. Sze, J.L. Moll, T. Sugano, Range-energy relation of hot electrons in gold, Solid-State Electron 7 (1964) 509–523.

[67] Y.K. Lee, H. Lee, C. Lee, E. Hwang, J.Y. Park, Hot-electron-based solar energy conversion with metal-semiconductor nanodiodes, J. Phys. Condens. Matter 28 (2016), 254006.

[68] J.R.M. Saavedra, A. Asenjo-Garcia, F.J. García, de Abajo, Hot-electron dynamics and thermalization in small metallic nanoparticles, ACS Photonics 3 (2016) 1637–1646.

[69] P. Panagiotopoulou, A. Christodoulakis, D.I. Kondarides, S. Boghosian, Particle size effects on the reducibility of titanium dioxide and its relation to the water–gas shift activity of Pt/TiO_2 catalysts, J. Catal. 240 (2006) 114–125.

[70] C. Zhang, H. He, K. Tanaka, Catalytic performance and mechanism of a Pt/TiO_2 catalyst for the oxidation of formaldehyde at room temperature, Appl. Catal. B 65 (2006) 37–43.

[71] P. Reyes, G. Pecchi, M. Morales, J.L.G. Fierro, The nature of the support and the metal precursor on the resistance to sulphur poisoning of Pt supported catalysts, Appl. Catal. A: Gen. 163 (1997) 145–152.

[72] W.S. Epling, P.K. Cheekatamarla, A.M. Lane, Reaction and surface characterization studies of titania-supported Co, Pt and Co/Pt catalysts for the selective oxidation of CO in H_2-containing streams, Chem. Eng. J. 93 (2003) 61–68.

[73] T. Huizinga, J. van Grondelle, R. Prins, A temperature programmed reduction study of Pt on Al_2O_3 and TiO_2, Appl. Catal. 10 (1984) 199–213.

[74] J.Z. Shyu, K. Otto, Characterization of Pt/γ-alumina catalysts containing ceria, J. Catal. 115 (1989) 16–23.

[75] F. Alonso, P. Riente, F. Rodríguez-Reinoso, J. Ruiz-Martínez, A. Sepúlveda-Escribano, M. Yus, Platinum nanoparticles supported on titania as an efficient hydrogen-transfer catalyst, J. Catal. 260 (2008) 113–118.

[76] Z. Liu, Y. Lu, L. Yuan, L. Ma, L. Zheng, J. Zhang, T. Hu, Selective catalytic reduction of NO_x with H_2 over WO_3 promoted Pt/TiO_2 catalyst, Appl. Catal. B 188 (2016) 189–197.

[77] J.C. Conesa, J. Soria, Reversible Ti^{3+} formation by hydrogen adsorption on M/anatase (TiO_2) catalysts, J. Phys. Chem. 86 (1982) 1392–1395.

[78] T. Nanba, C. Kohno, S. Masukawa, J. Uchisawa, N. Nakayama, A. Obuchi, Improvements in the N_2 selectivity of Pt catalysts in the NO–H_2–O_2 reaction at low temperatures, Appl. Catal. B 46 (2003) 353–364.

[79] F. Zuo, K. Bozhilov, R.J. Dillon, L. Wang, P. Smith, X. Zhao, C. Bardeen, P. Feng, Active facets on titanium(III)-doped TiO_2: an effective strategy to improve the visible-light photocatalytic activity, Angew. Chem. Int. Ed. 51 (2012) 6223–6226.

[80] M. Liu, X. Qiu, M. Miyauchi, K. Hashimoto, Cu(II) oxide amorphous nanoclusters grafted Ti^{3+} self-doped TiO_2: an efficient visible light photocatalyst, Chem. Mater. 23 (2011) 5282–5286.

[81] A. Pekkari, Z. Say, A. Susarrey-Arce, C. Langhammer, H. Härelind, V. Sebastian, K. Moth-Poulsen, Continuous microfluidic synthesis of Pd nanocubes and PdPt core–shell nanoparticles and their catalysis of NO_2 reduction, ACS Appl. Mater. Interfaces 11 (2019) 36196–36204.

[82] P. Christopher, H.L. Xin, S. Linic, Visible-light-enhanced catalytic oxidation reactions on plasmonic silver nanostructures, Nat. Chem. 3 (2011) 467–472.

[83] K. Qian, B.C. Sweeny, A.C. Johnston-Peck, W. Niu, J.O. Graham, J.S. DuChene, J. Qiu, Y.-C. Wang, M.H. Engelhard, D. Su, E.A. Stach, W. Wei, Surface plasmon-driven water reduction: gold nanoparticle size matters, J. Am. Chem. Soc. 136 (2014) 9842–9845.

[84] B. Seemala, A.J. Therrien, M. Lou, K. Li, J.P. Finzel, J. Qi, P. Nordlander, P. Christopher, Plasmon-mediated catalytic O_2 dissociation on Ag Nanostructures: Hot Electrons or near fields? ACS Energy Lett. 4 (2019) 1803–1809.

[85] C. Langhammer, B. Kasemo, I. Zoric, Absorption and scattering of light by Pt, Pd, Ag, and Au nanodisks: absolute cross sections and branching ratios, J. Chem. Phys. 126 (2007), 194702.

[86] C. Tiburski, A. Boje, S. Nilsson, Z. Say, J. Fritzsche, H. Ström, A. Hellman, C. Langhammer, A.C.S. Nano 15 (2021) 11535–11542.

[87] Y. Dubi, Y. Sivan, "Hot" electrons in metallic nanostructures—non-thermal carriers or heating? Light.: Sci. Appl. 8 (2019) 89.

[88] Y. Dubi, I.W. Un, Y. Sivan, Thermal effects - an alternative mechanism for plasmon-assisted photocatalysis, Chem. Sci. 11 (2020) 5017–5027.

[89] G. Baffou, I. Bordacchini, A. Baldi, R. Quidant, Simple experimental procedures to distinguish photothermal from hot-carrier processes in plasmonics, Light.: Sci. Appl. 9 (2020) 108.

[90] M.J. Kale, T. Avanesian, P. Christopher, Direct photocatalysis by plasmonic nanostructures, ACS Catal. 4 (2014) 116–128.

[91] P. Christopher, H.L. Xin, A. Marimuthu, S. Linic, Singular characteristics and unique chemical bond activation mechanisms of photocatalytic reactions on plasmonic nanostructures, Nat. Mater. 11 (2012) 1044–1050.